An Efficient A-FEM for Arbitrary Cracking in Solids

Qingda Yang[1,*], Wei Liu[1,2], and Xian-Yue Su[2]

[1] Dept. of Mechanical and Aerospace Engineering, University of Miami, Coral Gables, FL 33124. USA
[2] Dept. of Mechanics & Aerospace Engineering, Peking University, Beijing 100871, China
* Corresponding author: Tel: +1 305-284-3221; Email: qdyang@miami.edu

Abstract In this paper a new augmented finite element method (A-FEM) that can account for multiple, intra-elemental discontinuities in heterogeneous solids has been derived. It does not need the extra DoFs as in the extended finite element method (X-FEM), or the additional nodes as in the phantom node method (PNM). The new A-FEM employs four internal nodes to facilitate the calculation of subdomain stiffness and the crack displacements due to an intra-elemental discontinuity. It is shown that through a novel efficient solving algorithm the displacement DoFs associated with the internal nodes can be solved analytically as functions of the regular nodal DoFs for any piece-wise linear cohesive laws, which leads to a fully-condensed elemental equilibrium equation that is mathematically exact. The new formulation permits repeated elemental augmentation to include multiple interactive cracks within a single element, enabling a unified treatment of the evolution from a weak discontinuity, to a strong discontinuity, and to multiple intra-element discontinuities, all within a single element that employs standard DoFs only. The new A-FEM's capability in high-fidelity simulation of interactive cohesive cracks in homogeneous and heterogeneous solids has been demonstrated through several numerical examples. It has been demonstrated that the new A-FEM achieved more than two orders of magnitude improvement in numerical accuracy, efficiency, and robustness, compared to the X-FEM.

Keywords Augmented FEM, Extended FEM, Fracture, Cohesive model, Numerical simulation

1. Introduction

High-fidelity numerical simulation to the progressive damage evolution in complex heterogeneous materials such as composites remains a significant challenge despite decades of intensive research [1]. Heterogeneity poses special problems with the accurate prediction of local stress and strain fields, which can vary strongly with local material features; and with predicting cracks and localized damage bands, which can appear during damage evolution not only on the material boundaries, but also on other surfaces that cannot be specified *a priori*. The material heterogeneity issue cannot be resolved adequately by mainstream formulations of conventional materials/structures modeling, owing to the complex interaction between fiber tow architecture and constituent materials heterogeneity. One challenge is that many complex composites such as textiles are heterogeneous on the same scale as that of the features of the structures, which negates the common strategy of homogenizing the material properties in simulations. Furthermore, the structure will generally be subject to non-periodic mechanical and thermal loads, including spatial and temporal peaks.

The above challenges require the establishment of numerical modeling platforms that can deal with structural level performance with microscopic level resolution so that arbitrary local damage evolution, from their nucleation stage and coupled evolution to structurally critical dimensions, can be faithfully predicted. Traditional material degradation types of continuum mechanics based approaches are not likely to meet the challenges because the critical damage coupling information is lost during the homogenization process [2, 3]. Currently there are several promising methods that can deal with the material heterogeneity and the associated progressive damage issues. For example, the Peridynamics method [4, 5]. However, this method remains extremely computational intensive and its fidelity in dealing with complex material heterogeneity in 3D textiles has yet to be demonstrated. Another important class of numerical methods is the partition-of-unity based finite element methods (PUFEM[6], including the extended finite element method (X-FEM) [7-9] and the phantom node method (PNM) [10-14]. These methods are relatively mesh-independent and

computationally efficient when dealing with individual cracks. However, with these methods, tracing the evolution of complex fracture surfaces of multiple cracks quickly becomes extremely tedious and numerically burdensome [8, 15, 16].

Therefore, it is beneficial to seek numerical methods that can account for arbitrary discontinuities with less numerical burden for tracing complex crack surfaces. In this regard the embedded discontinuity FEM with internal DoFs is very promising [17-20]. This approach seeks to enrich the elemental strain field so that the discontinuity in strains or in displacements across a discontinuity can be represented. The additional DoFs associated with the crack displacements are then fully condensed at elemental level [19, 21]. However, this method suffers from possible stress locking because in many cases the assumed deformation modes are not permissible with the sub-domain element deformation modes. Furthermore, construction of an enhanced or augmented element with embedded multiple cracks to permit arbitrary crack merging and bifurcation becomes extremely tedious and difficult.

It is therefore highly desired to develop new finite element methods that can deal with discrete cracks without the need of introducing additional DoFs or nodes, so that the numerical burden for tracing crack surfaces can be minimized. In this paper, we present a new augmented finite element method (A-FEM) that can account for 1) intra-element material heterogeneity and 2) repeated elemental augmentation to enable multiple, interactive intra-element discontinuities. These capabilities are crucial to high-fidelity simulations of heterogeneous materials such as composites. In addition, we report a novel and efficient solving algorithm for elemental condensation that provides analytical solutions to the local equilibrium equations with embedded piece-wise linear cohesive crack like discontinuities. It will be demonstrated that the A-FEM empowered by the new condensation algorithm can provide orders of magnitude improvement in numerical efficiency, accuracy and robustness.

2. New A-FEM for Arbitrary, Multiple Cracking in Heterogeneous Solids

2.1 A-FE Formulation with Single Crack

Without the loss of generality, we choose the 4-node quadratic plane element to illustrate the augmented finite element scheme. The physical element with regular nodes 1, 2, 3, and 4 is severed by a cohesive crack (a strong discontinuity) or a bi-material interface (weak discontinuity) where the tractions are continuous but displacements are not. Figure 1 shows the two possible cut configurations. Instead of introducing two nodes with DoFs representing the assumed deformation modes (constant or linear) as in literature [19, 20], here we introduce 4 internal nodes (node No. 5, 6, 6' and 5' in Fig 1 (b & c)) with regular displacement DoFs so that the displacement jump is simply the difference between the respective node-pairs. As will be seen shortly this novel formulation allows us to derive accurate elemental equilibrium equations without the need to assume deformation modes, and more importantly, it offers the great advantage of permitting multiple intra-element discontinuities.

The internal nodes also facilitate the stiffness calculation of the sub-domains so that the equilibrium of the entire element can be expressed in general as the following.

$$\begin{bmatrix} [\mathbf{L}_{11}^{+}] & [\mathbf{L}_{12}^{+}] \\ [\mathbf{L}_{21}^{+}] & [\mathbf{L}_{22}^{+}] \end{bmatrix} \begin{Bmatrix} \mathbf{d}_{\text{ext}}^{+} \\ \mathbf{d}_{\text{int}}^{+} \end{Bmatrix} = \begin{Bmatrix} \mathbf{F}_{\text{ext}}^{+} \\ \mathbf{F}_{\text{int}}^{+} \end{Bmatrix} \quad (\text{for } \Omega^{+}); \quad \begin{bmatrix} [\mathbf{L}_{11}^{-}] & [\mathbf{L}_{12}^{-}] \\ [\mathbf{L}_{21}^{-}] & [\mathbf{L}_{22}^{-}] \end{bmatrix} \begin{Bmatrix} \mathbf{d}_{\text{ext}}^{-} \\ \mathbf{d}_{\text{int}}^{-} \end{Bmatrix} = \begin{Bmatrix} \mathbf{F}_{\text{ext}}^{-} \\ \mathbf{F}_{\text{int}}^{-} \end{Bmatrix} \quad (\text{for } \Omega^{-}) \quad (1)$$

where $\{\mathbf{d}_{\text{ext}}^{+}, \mathbf{d}_{\text{int}}^{+}\}^{\text{T}}$ and $\{\mathbf{d}_{\text{reg}}^{-}, \mathbf{d}_{\text{int}}^{-}\}^{\text{T}}$ are DoFs of the external or regular nodes and the internal nodes in the two subdomains, respectively. $\{\mathbf{F}_{\text{ext}}^{+}, \mathbf{F}_{\text{int}}^{+}\}^{\text{T}}$ and $\{\mathbf{F}_{\text{ext}}^{-}, \mathbf{F}_{\text{int}}^{-}\}^{\text{T}}$ are the nodal forces associated with regular and internal nodes; $[\mathbf{L}_{ij}^{+}]$ and $[\mathbf{L}_{ij}^{-}]$ $(i, j = 1, 2)$ are the stiffness sub-matrices of respective domains, which can be easily obtained with standard or subdomain integration schemes. The internal force arrays come from the integration of cohesive stresses along the crack surfaces, and,

due to stress continuity across the cohesive crack, $\mathbf{F}_{\text{int}}^{+} = \mathbf{F}_{6'5'}^{+} = -\mathbf{F}_{\text{int}}^{-} = -\mathbf{F}_{65}^{-}$. Note that, irrespective the cut configurations in Figure 1 (b) or (c), the internal displacements are always $\mathbf{d}_{\text{int}}^{+} = \mathbf{d}_{6'5'}; \mathbf{d}_{\text{int}}^{-} = \mathbf{d}_{65}$.

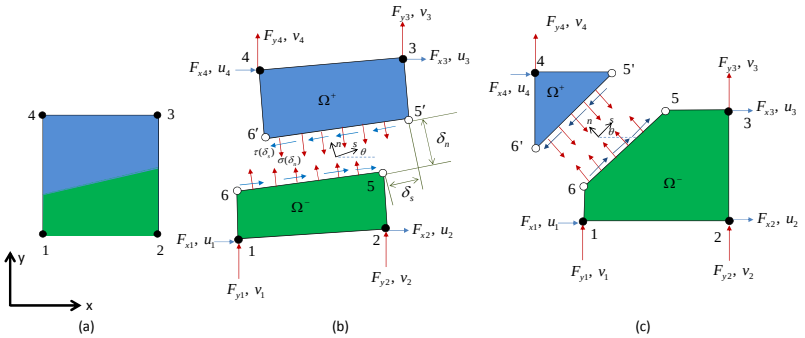

Figure 1 Illustration of the element augmentation from a regular element with possible different material domains (a), to an A-FE with two rectangular sub-domains (b), or to an A-FE with one triangular sub-domain and one pentagon sub-domain (c).

For the piece-wise linear cohesive laws shown in Figure 2, the cohesive stresses as functions of crack displacements can be written as

$$\begin{aligned} &\sigma(\delta_n) = \hat{\sigma}^{(i-1)} + \alpha_n^{(i)}(\delta_n - \delta_n^{(i-1)}) \qquad (\delta_n \subset [\delta_n^{(i-1)}, \delta_n^{(i)}] \qquad (i = 1,2,\cdots 4) \\ &\tau(\delta_s) = \text{sgn}(\delta_s)\left[\hat{\tau}^{(j-1)} + \alpha_s^{(j)}\left(|\delta_s| - \delta_s^{(j-1)}\right)\right] \quad (|\delta_s| \subset [\delta_s^{(i-1)}, \delta_s^{(i)}] \quad (j = 1,2,\cdots 4) \end{aligned} \tag{2}$$

where sgn(·) is a sign function, and |·| denotes absolute value; $\sigma(\delta_n)$ and $\tau(\delta_s)$ are normal and tangential tractions along the cohesive crack; δ_n and δ_s are normal and tangential crack displacement; the superscripts *i* and *j* denote the linear segment number as labeled in Figure 2. $\hat{\sigma}^{(i)}$ and $\hat{\tau}^{(j)}$, $\delta_n^{(i)}$ and $\delta_s^{(j)}$, $\alpha_n^{(i)}$ and $\alpha_s^{(j)}$ are the characteristic stresses, crack displacements, and slopes (Fig 2), and $\hat{\sigma}^{(0)} = \hat{\tau}^{(0)} = 0$ and $\delta_n^{(0)} = \delta_s^{(0)} = 0$.

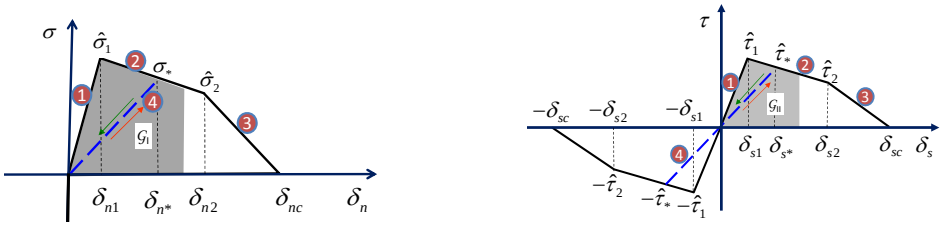

(a) mode I cohesive law (b) mode II cohesive law

Figure 2 Mixed-mode cohesive model with piece-wise linear traction-separation laws used in this study

The propagation criterion used for the cohesive crack is one that has been widely used and validated in literature [22, 23]

$$\mathcal{G}_{\text{I}}^{*} / \Gamma_{\text{I}} + \mathcal{G}_{\text{II}}^{*} / \Gamma_{\text{II}} = 1 \tag{3}$$

where $\mathcal{G}_{\text{I}}^{*}$ and $\mathcal{G}_{\text{II}}^{*}$ are the energy dissipations at which the cohesive failure occurs (shaded areas in Fig 2), and Γ_{I} and Γ_{II} are the <u>total</u> areas under the pure opening and pure shear traction-separation laws.

With the above piece-wise linear cohesive law, the cohesive stresses between the two pairs of internal nodes 5-5' and 6-6' are known. The internal force arrays $\mathbf{F}_{65}$ and $\mathbf{F}_{6'5'}$ are the cohesive stresses integrated over the crack surfaces and transfer them into global coordinates,

$$\mathbf{F}_{65} = -\mathbf{F}_{6'5'} = l_e^{\theta}(\mathbf{S}_0 + \boldsymbol{\alpha}\{\Delta\mathbf{d}_{66'}, \Delta\mathbf{d}_{55'}\}^{\text{T}}) \tag{4}$$

where $\Delta\mathbf{d}_{6'6} = \mathbf{d}_{6'} - \mathbf{d}_6$ and $\Delta\mathbf{d}_{5'5} = \mathbf{d}_{5'} - \mathbf{d}_5$. $\mathbf{S}_0$ and $\boldsymbol{\alpha}$ are the matrices determined by the characteristic cohesive stresses and slopes. Substituting Eqn (4) to Eqn (1) the following is derived

$$\begin{Bmatrix}\mathbf{d}_{6'5'}\\ \mathbf{d}_{65}\end{Bmatrix}=\begin{bmatrix}-l_{e1}\mathbf{A}^{-1}\left(\mathbf{I}-l_{e1}\boldsymbol{\alpha}(\boldsymbol{\Psi}_{22}^{-})^{-1}\right) & \mathbf{0}\\ \mathbf{0} & l_{e1}\mathbf{B}^{-1}\left(\mathbf{I}-l_{e1}\boldsymbol{\alpha}(\boldsymbol{\Psi}_{22}^{+})^{-1}\right)\end{bmatrix}\begin{Bmatrix}\mathbf{S}_0\\ \mathbf{S}_0\end{Bmatrix}+\begin{bmatrix}-l_{e1}\mathbf{A}^{-1}\boldsymbol{\alpha}(\boldsymbol{\Psi}_{22}^{-})^{-1}\mathbf{L}_{21}^{-} & -\mathbf{A}^{-1}\mathbf{L}_{21}^{+}\\ -\mathbf{B}^{-1}\mathbf{L}_{21}^{-} & -l_{e1}\mathbf{B}^{-1}\boldsymbol{\alpha}(\boldsymbol{\Psi}_{22}^{+})^{-1}\mathbf{L}_{21}^{+}\end{bmatrix}\begin{Bmatrix}\mathbf{d}_{ext}^{-}\\ \mathbf{d}_{ext}^{+}\end{Bmatrix} \tag{5}$$

where $\boldsymbol{\Psi}_{22}^{+}=\mathbf{L}_{22}^{+}+l_{e1}\boldsymbol{\alpha};\boldsymbol{\Psi}_{22}^{-}=\mathbf{L}_{22}^{-}+l_{e1}\boldsymbol{\alpha};\mathbf{A}=\boldsymbol{\Psi}_{22}^{+}-l_{e1}{}^{2}\boldsymbol{\alpha}(\boldsymbol{\Psi}_{22}^{-})^{-1}\boldsymbol{\alpha};\ \mathbf{B}=\boldsymbol{\Psi}_{22}^{-}-l_{e1}{}^{2}\boldsymbol{\alpha}(\boldsymbol{\Psi}_{22}^{+})^{-1}\boldsymbol{\alpha}$, and $\mathbf{I}$ is the identity matrix. Substituting Eqn (5) it into Eqn (1) the full condensed equilibrium is obtained,

$$\begin{bmatrix}\mathbf{L}_{11}^{-}-\mathbf{L}_{12}^{-}\mathbf{B}^{-1}\mathbf{L}_{21}^{-} & -l_{e1}\mathbf{L}_{12}^{-}\mathbf{B}^{-1}\boldsymbol{\alpha}(\boldsymbol{\Psi}_{22}^{+})^{-1}\mathbf{L}_{21}^{+}\\ -l_{e1}\mathbf{L}_{12}^{+}\mathbf{A}^{-1}\boldsymbol{\alpha}(\boldsymbol{\Psi}_{22}^{-})^{-1}\mathbf{L}_{21}^{-} & \mathbf{L}_{11}^{+}-\mathbf{L}_{12}^{+}\mathbf{A}^{-1}\mathbf{L}_{21}^{+}\end{bmatrix}\begin{Bmatrix}\mathbf{d}_{ext}^{-}\\ \mathbf{d}_{ext}^{+}\end{Bmatrix}=\begin{Bmatrix}\mathbf{F}_{ext}^{-}\\ \mathbf{F}_{ext}^{+}\end{Bmatrix}-\begin{bmatrix}l_{e1}\mathbf{L}_{12}^{-}\mathbf{B}^{-1}\left(\mathbf{I}-l_{e1}\boldsymbol{\alpha}(\boldsymbol{\Psi}_{22}^{+})^{-1}\right) & 0\\ 0 & -l_{e1}\mathbf{L}_{12}^{+}\mathbf{A}^{-1}\left(\mathbf{I}-l_{e1}\boldsymbol{\alpha}(\boldsymbol{\Psi}_{22}^{-})^{-1}\right)\end{bmatrix}\begin{Bmatrix}\mathbf{S}_0\\ \mathbf{S}_0\end{Bmatrix} \tag{6}$$

Elemental Condensation Algorithm

Eqn (6) is nonlinear due to the nonlinearity from the cohesive laws. In the literature, Newton-Raphson method [19, 20] (or its modified variants) has been used to solve this equation iteratively. However, our novel derivation above has yielded an explicit expression between the displacements of the internal nodes and those of the external nodes, i.e., Eqn (5). We have proved that, for any piece-wise linear cohesive laws, $\mathbf{d}_{6'5'}$ and $\mathbf{d}_{65}$ can be uniquely determined with mathematical exactness through a very simple yet efficient algorithm. The algorithm solves Eqn (5) by consistent check between trial cohesive slopes and the resulted crack displacements. Once Eqn (5) is solved, the matrices $[\boldsymbol{\beta}]$, $[\mathbf{K}_{22}^{+}]$, and $[\mathbf{K}_{22}^{-}]$ are all determined and elemental equilibrium of Eqn (6) is determined with mathematical rigor. This novel way of solving the crack displacements has never been reported in literature and we later show that it leads to orders of magnitude improvement on numerical efficiency.

2.2 A-FE Formulation with Two Interactive Cracks

In such a case, there are altogether three basic cracking configurations as shown in Fig 3(a), Fig 3(b) and Fig3(c), where l_{e1} is the first crack length and l_{e2} is the second crack length. The second crack intersects and cuts the first crack into two segments with length γl_{e1} (left) and $(1-\gamma)l_{e1}$ (right). Despite the different crack configurations in Figure 3, the internal DoF and force arrays can be arranged in a unified way as below.

$$\mathbf{d}_{\text{int}}^{+}=\mathbf{d}_{6'5'};\ \mathbf{d}_{\text{int}}^{r-}=\mathbf{d}_{58'7'};\ \mathbf{d}_{\text{int}}^{l-}=\mathbf{d}_{786}\qquad \mathbf{F}_{\text{int}}^{+}=\mathbf{F}_{6'5'};\ \mathbf{F}_{\text{int}}^{r-}=\mathbf{F}_{58'7'};\ \mathbf{F}_{\text{int}}^{l-}=\mathbf{F}_{786} \tag{7}$$

This enables a unified expression for the equilibrium of all three subdomains as follows

$$\begin{cases}\begin{bmatrix}\mathbf{L}_{11}^{+} & \mathbf{L}_{12}^{+}\\ \mathbf{L}_{21}^{+} & \mathbf{L}_{22}^{+}\end{bmatrix}\begin{Bmatrix}\mathbf{d}_{ext}^{+}\\ \mathbf{d}_{6'5'}\end{Bmatrix}=\begin{Bmatrix}\mathbf{F}_{ext}^{+}\\ \mathbf{F}_{6'5'}\end{Bmatrix} & \text{(a)}\\ & \text{(b)}\end{cases}\quad(\text{for }\Omega^{+})$$

$$\begin{cases}\begin{bmatrix}\mathbf{L}_{11}^{r-} & \mathbf{L}_{12}^{r-}\\ \mathbf{L}_{21}^{r-} & \mathbf{L}_{22}^{r-}\end{bmatrix}\begin{Bmatrix}\mathbf{d}_{ext}^{r-}\\ \mathbf{d}_{58'7'}\end{Bmatrix}=\begin{Bmatrix}\mathbf{F}_{ext}^{r-}\\ \mathbf{F}_{58'7'}\end{Bmatrix} & \text{(c)}\\ & \text{(d)}\end{cases}\quad(\text{for }\Omega^{r-}) \tag{8}$$

$$\begin{cases}\begin{bmatrix}\mathbf{L}_{11}^{l-} & \mathbf{L}_{12}^{l-}\\ \mathbf{L}_{21}^{l-} & \mathbf{L}_{22}^{l-}\end{bmatrix}\begin{Bmatrix}\mathbf{d}_{ext}^{l-}\\ \mathbf{d}_{786}\end{Bmatrix}=\begin{Bmatrix}\mathbf{F}_{ext}^{l-}\\ \mathbf{F}_{786}\end{Bmatrix} & \text{(e)}\\ & \text{(f)}\end{cases}\quad(\text{for }\Omega^{l-})$$

Here, the sub-matrices ($\mathbf{L}_{ij}^{l-}, \mathbf{L}_{ij}^{r-}$, and $\mathbf{L}_{ij}^{+}$ $(i, j = 1, 2)$) are the stiffness matrices of the subdomains Ω^{+}, $\Omega^{r-}$and Ω^{l-}, respectively. To integrate the cohesive stress along the three cohesive crack segments into respective internal nodal forces, the first order Gaussian Integration scheme was used on each of the three cracked segments. The integration points are at the center of each crack

segment as indicated in Figure 3(b) by the solid dots labeled by I, II, and III.

The relation between these cohesive stresses and the internal nodal displacements is

$$\begin{cases} \left\{\tau_{\mathrm{I}}^{(i)}, \sigma_{\mathrm{I}}^{(j)}\right\}^{\mathbf{T}} = \boldsymbol{\sigma}_{0\mathrm{I}} + \boldsymbol{\alpha}_{0\mathrm{I}}\mathbf{R}_1\left((1-\gamma/2)\mathbf{d}_{6'} + (\gamma/2)\mathbf{d}_{5'}\right) - \boldsymbol{\alpha}_{0\mathrm{I}}\mathbf{R}_1\left(\mathbf{d}_6 + \mathbf{d}_8\right)/2 \\ \left\{\tau_{\mathrm{II}}^{(k)}, \sigma_{\mathrm{II}}^{(l)}\right\}^{\mathbf{T}} = \boldsymbol{\sigma}_{0\mathrm{II}} + \boldsymbol{\alpha}_{0\mathrm{II}}\mathbf{R}_1\left((1-\gamma/2)\mathbf{d}_{6'} + (1+\gamma/2)\mathbf{d}_{5'}\right) - \boldsymbol{\alpha}_{0\mathrm{II}}\mathbf{R}_1\left(\mathbf{d}_5 + \mathbf{d}_{8'}\right)/2 \\ \left\{\tau_{\mathrm{III}}^{(m)}, \sigma_{\mathrm{III}}^{(n)}\right\}^{\mathbf{T}} = \boldsymbol{\sigma}_{0\mathrm{III}} + \boldsymbol{\alpha}_{0\mathrm{III}}\mathbf{R}_2\left(\mathbf{d}_{7'} + \mathbf{d}_{8'}\right)/2 - \boldsymbol{\alpha}_{0\mathrm{III}}\mathbf{R}_2\left(\mathbf{d}_7 + \mathbf{d}_8\right)/2 \end{cases} \tag{9}$$

where

$$\boldsymbol{\sigma}_{0\mathrm{I}} = \begin{Bmatrix} \hat{\tau}^{(i)} - \alpha_s^{(i)}\delta_s^{(i)} \\ \hat{\sigma}^{(j)} - \alpha_n^{(j)}\delta_n^{(j)} \end{Bmatrix}; \quad \boldsymbol{\sigma}_{0\mathrm{II}} = \begin{Bmatrix} \hat{\tau}^{(k)} - \alpha_s^{(k)}\delta_s^{(k)} \\ \hat{\sigma}^{(l)} - \alpha_n^{(l)}\delta_n^{(l)} \end{Bmatrix}; \quad \boldsymbol{\sigma}_{0\mathrm{III}} = \begin{Bmatrix} \hat{\tau}^{(m)} - \alpha_s^{(m)}\delta_s^{(m)} \\ \hat{\sigma}^{(n)} - \alpha_n^{(n)}\delta_n^{(n)} \end{Bmatrix}$$

$$\boldsymbol{\alpha}_{0\mathrm{I}} = \mathrm{Diag}[\alpha_s^{(i)}; \alpha_n^{(j)}]; \quad \boldsymbol{\alpha}_{0\mathrm{II}} = \mathrm{Diag}[\alpha_s^{(k)}; \alpha_n^{(l)}]; \quad \boldsymbol{\alpha}_{0\mathrm{III}} = \mathrm{Diag}[\alpha_s^{(m)}; \alpha_n^{(n)}];$$

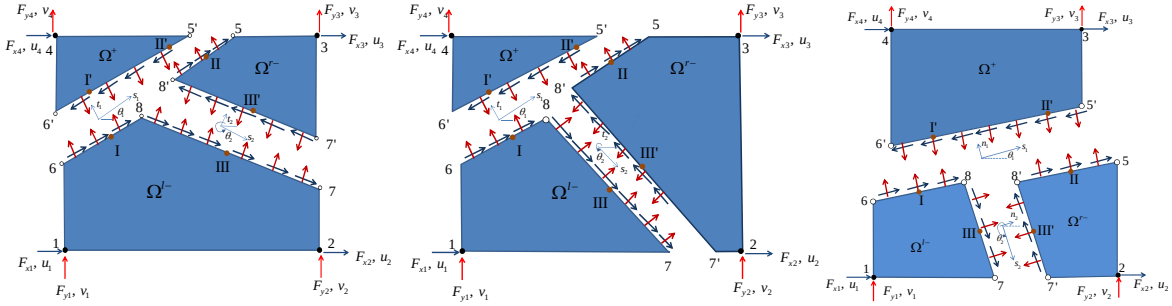

(a) (b) (c)

Figure 3 Illustration of a 2D A-FE with two intra-elemental cracks (3 subdomains)

The internal forces, $\{\mathbf{F}_{6'5'}\}$, $\{\mathbf{F}_{58'7'}\}$, and $\{\mathbf{F}_{786}\}$, integrated from the cohesive stresses along the respective crack lengths are

$$\begin{cases} \mathbf{F}_{6'5'} = \mathbf{T}_{\mathbf{R}}^{+}\left\{\tau_{\mathrm{I}}^{(i)}, \quad \sigma_{\mathrm{I}}^{(j)}, \quad \tau_{\mathrm{II}}^{(k)}, \quad \sigma_{\mathrm{II}}^{(l)}\right\}^{\mathbf{T}} \\ \mathbf{F}_{786} = \mathbf{T}_{\mathbf{R}}^{l-}\left\{\tau_{\mathrm{I}}^{(i)}, \quad \sigma_{\mathrm{I}}^{(j)}, \quad \tau_{\mathrm{III}}^{(m)}, \quad \sigma_{\mathrm{III}}^{(n)}\right\}^{\mathbf{T}} \\ \mathbf{F}_{58'7'} = \mathbf{T}_{\mathbf{R}}^{r-}\left\{\tau_{\mathrm{I}}^{(k)}, \quad \sigma_{\mathrm{I}}^{(l)}, \quad \tau_{\mathrm{III}}^{(m)}, \quad \sigma_{\mathrm{III}}^{(n)}\right\}^{\mathbf{T}} \end{cases} \tag{10}$$

where $\mathbf{T}_{\mathbf{R}}^{+}$, $\mathbf{T}_{\mathbf{R}}^{l-}$, and $\mathbf{T}_{\mathbf{R}}^{r-}$ are the respective integration matrices:

$$\mathbf{T}_{\mathbf{R}}^{+} = -\frac{1}{2}\begin{bmatrix} \gamma(2-\gamma)l_{e1}\mathbf{R}_1^{\mathbf{T}} & (1-\gamma)^2 l_{e1}\mathbf{R}_1^{\mathbf{T}} \\ \gamma^2 l_{e1}\mathbf{R}_1^{\mathbf{T}} & (1-\gamma^2)l_{e1}\mathbf{R}_1^{\mathbf{T}} \end{bmatrix};$$

$$\mathbf{T}_{\mathbf{R}}^{l-} = \frac{1}{2}\begin{bmatrix} \mathbf{0} & l_{e2}\mathbf{R}_2^{\mathbf{T}} \\ \gamma l_{e1}\mathbf{R}_1^{\mathbf{T}} & l_{e2}\mathbf{R}_2^{\mathbf{T}} \\ \gamma l_{e1}\mathbf{R}_1^{\mathbf{T}} & \mathbf{0} \end{bmatrix}; \quad \mathbf{T}_{\mathbf{R}}^{r-} = \frac{1}{2}\begin{bmatrix} (1-\gamma)l_{e1}\mathbf{R}_1^{\mathbf{T}} & \mathbf{0} \\ (1-\gamma)l_{e1}\mathbf{R}_1^{\mathbf{T}} & -l_{e2}\mathbf{R}_2^{\mathbf{T}} \\ \mathbf{0} & -l_{e2}\mathbf{R}_2^{\mathbf{T}} \end{bmatrix} \tag{11}$$

Substituting Eqn (9) into (10) and then Eqn (8), the internal crack displacements can be derived as

$$\begin{Bmatrix} \mathbf{d}_{6'5'} \\ \mathbf{d}_{786} \\ \mathbf{d}_{58'7'} \end{Bmatrix} = \begin{bmatrix} \mathbf{Y}_7 & \mathbf{Y}_8 & \mathbf{Y}_9 \\ \mathbf{Y}_4 & \mathbf{Y}_5 & \mathbf{Y}_6 \\ \mathbf{Y}_1 & \mathbf{Y}_2 & \mathbf{Y}_3 \end{bmatrix}\begin{Bmatrix} \mathbf{S}_1 \\ \mathbf{S}_2 \\ \mathbf{S}_3 \end{Bmatrix} + \begin{bmatrix} \mathbf{X}_{13} & \mathbf{X}_{14} & \mathbf{X}_{15} \\ \mathbf{X}_{10} & \mathbf{X}_{11} & \mathbf{X}_{12} \\ \mathbf{X}_7 & \mathbf{X}_8 & \mathbf{X}_9 \end{bmatrix}\begin{Bmatrix} \mathbf{d}_{ext}^{l-} \\ \mathbf{d}_{ext}^{r-} \\ \mathbf{d}_{ext}^{+} \end{Bmatrix} \tag{12}$$

where $\mathbf{S}_1 = \mathbf{T}_{\mathbf{R}}^{+}\left\{\boldsymbol{\sigma}_{0\mathrm{I}}, \boldsymbol{\sigma}_{0\mathrm{II}}\right\}^{\mathbf{T}}$, $\mathbf{S}_2 = \mathbf{T}_{\mathbf{R}}^{l-}\left\{\boldsymbol{\sigma}_{0\mathrm{I}}, \boldsymbol{\sigma}_{0\mathrm{III}}\right\}^{\mathbf{T}}$, $\mathbf{S}_3 = \mathbf{T}_{\mathbf{R}}^{r-}\left\{\boldsymbol{\sigma}_{0\mathrm{II}}, \boldsymbol{\sigma}_{0\mathrm{III}}\right\}^{\mathbf{T}}$;

$$\mathbf{X}_1 = \mathbf{L}_{22}^{+} - \boldsymbol{\alpha}_{11}; \qquad \mathbf{X}_2 = \mathbf{L}_{22}^{l-} - \boldsymbol{\alpha}_{22} - \boldsymbol{\alpha}_{21}(\mathbf{X}_1)^{-1}\boldsymbol{\alpha}_{12};$$

$$\mathbf{X}_3 = -\boldsymbol{\alpha}_{21}(\mathbf{X}_1)^{-1}\boldsymbol{\alpha}_{13} - \boldsymbol{\alpha}_{23}; \qquad \mathbf{X}_4 = -\boldsymbol{\alpha}_{31}(\mathbf{X}_1)^{-1}\boldsymbol{\alpha}_{12} - \boldsymbol{\alpha}_{32};$$

$$\mathbf{X}_5 = \mathbf{L}_{22}^{r-} - \boldsymbol{\alpha}_{33} - \boldsymbol{\alpha}_{31}(\mathbf{X}_1)^{-1}\boldsymbol{\alpha}_{13}; \qquad \mathbf{X}_6 = \mathbf{X}_5 - \mathbf{X}_4(\mathbf{X}_2)^{-1}\mathbf{X}_3$$

$$\mathbf{X}_7 = (\mathbf{X}_6)^{-1}\mathbf{X}_4(\mathbf{X}_2)^{-1}\mathbf{L}_{21}^{l-}; \qquad \mathbf{X}_8 = -(\mathbf{X}_6)^{-1}\mathbf{L}_{21}^{r-};$$

$$\mathbf{X}_9 = (\mathbf{X}_6)^{-1}\left(\mathbf{X}_4(\mathbf{X}_2)^{-1}\boldsymbol{\alpha}_{21} - \boldsymbol{\alpha}_{31}\right)(\mathbf{X}_1)^{-1}\mathbf{L}_{21}^{+}$$

$$\mathbf{X}_{10} = -(\mathbf{X}_2)^{-1}\left(\mathbf{X}_3\mathbf{X}_7 + \mathbf{L}_{21}^{l-}\right); \qquad \mathbf{X}_{11} = -(\mathbf{X}_2)^{-1}\mathbf{X}_3\mathbf{X}_8;$$

$$\mathbf{X}_{12} = -(\mathbf{X}_2)^{-1}\left(\mathbf{X}_3\mathbf{X}_9 + \boldsymbol{\alpha}_{21}(\mathbf{X}_1)^{-1}\mathbf{L}_{21}^{+}\right) \qquad \mathbf{X}_{13} = (\mathbf{X}_1)^{-1}\left(\boldsymbol{\alpha}_{13}\mathbf{X}_7 + \boldsymbol{\alpha}_{12}\mathbf{X}_{10}\right);$$

$$\mathbf{X}_{14} = (\mathbf{X}_1)^{-1}\left(\boldsymbol{\alpha}_{13}\mathbf{X}_8 + \boldsymbol{\alpha}_{12}\mathbf{X}_{11}\right); \qquad \mathbf{X}_{15} = (\mathbf{X}_1)^{-1}\left(-\mathbf{L}_{21}^{+} + \boldsymbol{\alpha}_{13}\mathbf{X}_9 + \boldsymbol{\alpha}_{12}\mathbf{X}_{12}\right)$$

$$\mathbf{Y}_1 = (\mathbf{X}_6)^{-1}\left(\boldsymbol{\alpha}_{31} - \mathbf{X}_4(\mathbf{X}_2)^{-1}\boldsymbol{\alpha}_{21}\right)(\mathbf{X}_1)^{-1}; \qquad \mathbf{Y}_2 = -(\mathbf{X}_6)^{-1}\mathbf{X}_4(\mathbf{X}_2)^{-1};$$

$$\mathbf{Y}_3 = (\mathbf{X}_6)^{-1} \qquad \mathbf{Y}_4 = (\mathbf{X}_2)^{-1}\left(\boldsymbol{\alpha}_{21}(\mathbf{X}_1)^{-1} - \mathbf{X}_3\mathbf{Y}_1\right);$$

$$\mathbf{Y}_5 = (\mathbf{X}_2)^{-1}\left(\mathbf{I} - \mathbf{X}_3\mathbf{Y}_2\right); \qquad \mathbf{Y}_6 = -(\mathbf{X}_2)^{-1}\mathbf{X}_3\mathbf{Y}_3;$$

$$\mathbf{Y}_7 = (\mathbf{X}_1)^{-1}\left(\mathbf{I} + \boldsymbol{\alpha}_{13}\mathbf{Y}_1 + \boldsymbol{\alpha}_{12}\mathbf{Y}_4\right); \qquad \mathbf{Y}_8 = (\mathbf{X}_1)^{-1}\left(\boldsymbol{\alpha}_{13}\mathbf{Y}_2 + \boldsymbol{\alpha}_{12}\mathbf{Y}_5\right);$$

$$\mathbf{Y}_9 = (\mathbf{X}_1)^{-1}\left(\boldsymbol{\alpha}_{13}\mathbf{Y}_3 + \boldsymbol{\alpha}_{12}\mathbf{Y}_6\right)$$

$$\boldsymbol{\alpha}_{11} = \frac{1}{2}\mathbf{T}_{\mathbf{R}}^{+}\begin{bmatrix}(2-\gamma)\boldsymbol{\alpha}_{0\mathrm{I}}\mathbf{R}_1 & \gamma\boldsymbol{\alpha}_{0\mathrm{I}}\mathbf{R}_1 \\ (1-\gamma)\boldsymbol{\alpha}_{0\mathrm{II}}\mathbf{R}_1 & (1+\gamma)\boldsymbol{\alpha}_{0\mathrm{II}}\mathbf{R}_1\end{bmatrix}; \qquad \boldsymbol{\alpha}_{12} = \frac{1}{2}\mathbf{T}_{\mathbf{R}}^{+}\begin{bmatrix}\mathbf{0} & -\boldsymbol{\alpha}_{0\mathrm{I}}\mathbf{R}_1 & -\boldsymbol{\alpha}_{0\mathrm{I}}\mathbf{R}_1 \\ \mathbf{0} & \mathbf{0} & \mathbf{0}\end{bmatrix};$$

$$\boldsymbol{\alpha}_{13} = \frac{1}{2}\mathbf{T}_{\mathbf{R}}^{+}\begin{bmatrix}\mathbf{0} & \mathbf{0} & \mathbf{0} \\ -\boldsymbol{\alpha}_{0\mathrm{II}}\mathbf{R}_1 & -\boldsymbol{\alpha}_{0\mathrm{II}}\mathbf{R}_1 & \mathbf{0}\end{bmatrix}; \qquad \boldsymbol{\alpha}_{21} = \frac{1}{2}\mathbf{T}_{\mathbf{R}}^{l-}\begin{bmatrix}(2-\gamma)\boldsymbol{\alpha}_{0\mathrm{I}}\mathbf{R}_1 & \gamma\boldsymbol{\alpha}_{0\mathrm{I}}\mathbf{R}_1 \\ \mathbf{0} & \mathbf{0}\end{bmatrix};$$

$$\boldsymbol{\alpha}_{22} = \frac{1}{2}\mathbf{T}_{\mathbf{R}}^{l-}\begin{bmatrix}\mathbf{0} & -\boldsymbol{\alpha}_{0\mathrm{I}}\mathbf{R}_1 & -\boldsymbol{\alpha}_{0\mathrm{I}}\mathbf{R}_1 \\ -\boldsymbol{\alpha}_{0\mathrm{III}}\mathbf{R}_2 & -\boldsymbol{\alpha}_{0\mathrm{III}}\mathbf{R}_2 & \mathbf{0}\end{bmatrix}; \qquad \boldsymbol{\alpha}_{23} = \frac{1}{2}\mathbf{T}_{\mathbf{R}}^{l-}\begin{bmatrix}\mathbf{0} & \mathbf{0} & \mathbf{0} \\ \mathbf{0} & \boldsymbol{\alpha}_{0\mathrm{III}}\mathbf{R}_2 & \boldsymbol{\alpha}_{0\mathrm{III}}\mathbf{R}_2\end{bmatrix};$$

$$\boldsymbol{\alpha}_{31} = \frac{1}{2}\mathbf{T}_{\mathbf{R}}^{r-}\begin{bmatrix}(1-\gamma)\boldsymbol{\alpha}_{0\mathrm{II}}\mathbf{R}_1 & (1+\gamma)\boldsymbol{\alpha}_{0\mathrm{II}}\mathbf{R}_1 \\ \mathbf{0} & \mathbf{0}\end{bmatrix}; \qquad \boldsymbol{\alpha}_{32} = \frac{1}{2}\mathbf{T}_{\mathbf{R}}^{r-}\begin{bmatrix}\mathbf{0} & \mathbf{0} & \mathbf{0} \\ -\boldsymbol{\alpha}_{0\mathrm{III}}\mathbf{R}_2 & -\boldsymbol{\alpha}_{0\mathrm{III}}\mathbf{R}_2 & \mathbf{0}\end{bmatrix};$$

$$\boldsymbol{\alpha}_{33} = \frac{1}{2}\mathbf{T}_{\mathbf{R}}^{r-}\begin{bmatrix}-\boldsymbol{\alpha}_{0\mathrm{II}}\mathbf{R}_1 & -\boldsymbol{\alpha}_{0\mathrm{II}}\mathbf{R}_1 & \mathbf{0} \\ \mathbf{0} & \boldsymbol{\alpha}_{0\mathrm{III}}\mathbf{R}_2 & \boldsymbol{\alpha}_{0\mathrm{III}}\mathbf{R}_2\end{bmatrix}$$

Finally, by substituting Eqn (12) into expressions (a, c, e) in Eqn (8) to eliminate the internal nodal displacements, the fully condensed elemental equilibrium equation is obtained as

$$\begin{bmatrix}\mathbf{L}_{11}^{l-} + \mathbf{L}_{12}^{l-}\mathbf{X}_{10} & \mathbf{L}_{12}^{l-}\mathbf{X}_{11} & \mathbf{L}_{12}^{l-}\mathbf{X}_{12} \\ \mathbf{L}_{12}^{r-}\mathbf{X}_7 & \mathbf{L}_{11}^{r-} + \mathbf{L}_{12}^{r-}\mathbf{X}_8 & \mathbf{L}_{12}^{r-}\mathbf{X}_9 \\ \mathbf{L}_{12}^{+}\mathbf{X}_{13} & \mathbf{L}_{12}^{+}\mathbf{X}_{14} & \mathbf{L}_{11}^{+} + \mathbf{L}_{12}^{+}\mathbf{X}_{15}\end{bmatrix}\begin{Bmatrix}\mathbf{d}_{ext}^{l-} \\ \mathbf{d}_{ext}^{r-} \\ \mathbf{d}_{ext}^{+}\end{Bmatrix} = \begin{Bmatrix}\mathbf{F}_{ext}^{l-} \\ \mathbf{F}_{ext}^{r-} \\ \mathbf{F}_{ext}^{+}\end{Bmatrix} - \begin{bmatrix}\mathbf{L}_{12}^{l-}\mathbf{Y}_4 & \mathbf{L}_{12}^{l-}\mathbf{Y}_5 & \mathbf{L}_{12}^{l-}\mathbf{Y}_6 \\ \mathbf{L}_{12}^{r-}\mathbf{Y}_1 & \mathbf{L}_{12}^{r-}\mathbf{Y}_2 & \mathbf{L}_{12}^{r-}\mathbf{Y}_3 \\ \mathbf{L}_{12}^{+}\mathbf{Y}_7 & \mathbf{L}_{12}^{+}\mathbf{Y}_8 & \mathbf{L}_{12}^{+}\mathbf{Y}_9\end{bmatrix}\begin{Bmatrix}\mathbf{S}_1 \\ \mathbf{S}_2 \\ \mathbf{S}_3\end{Bmatrix} \quad (13)$$

Note that Eqn (12) and Eqn (13) share the same matrices $\mathbf{X}_p$ (p = 1, 2, …15), $\mathbf{Y}_q$ (q = 1, 2,…9),), and $\boldsymbol{S}_r$ (r = 1, ..3), which are all functions of the characteristic cohesive stresses ($\boldsymbol{\sigma}_{0\mathrm{I}}, \boldsymbol{\sigma}_{0\mathrm{II}}$, and $\boldsymbol{\sigma}_{0\mathrm{III}}$) and the cohesive stiffnesses ($\boldsymbol{\alpha}_{0\mathrm{I}}, \boldsymbol{\alpha}_{0\mathrm{II}}$, and $\boldsymbol{\alpha}_{0\mathrm{III}}$) (Eqn 9). The same elemental condensation procedure in section 2.1 applies to Eqn (12) and, once the solution is found, $\mathbf{X}_p$, $\mathbf{Y}_q$, $\boldsymbol{S}_r$ are all established. Substituting them into Eqn (13) the fully condensed elemental equilibrium is then satisfied with mathematical exactness.

3. A-FEM Simulated 4PSB Test and Compared with X-FEM

In this section, the capabilities of the proposed A-FEM is first evaluated by simulating the crack propagation in a 4-point shear beam (4PSB) test reported in [24]. The problem has been simulated

by Moes and Belytschko in [7] using the X-FEM with a non-structured triangular mesh. The numerical model setup used in [7] is reproduced in Figure 4(a). The geometry dimensions are: b = 200 mm; l/b = 4; a/b = 0.2; c/b = 0.4; $l_1 = l_2$ = 20 mm; t = 100 mm.

As in [7], the maximum principal stress criterion was used for crack initiation and the cohesive parmaeters for the concrete material are identical to those used in [7].

To investigate the mesh sensitivity of the present A-FEM, the problem was analyzed by five different structured meshes with characteristic mesh size of h = 2, 4, 8, 13.3, and 20 mm (the total elements are 10760, 2849, 1094, 640, and 410, respectively), and two unstructured meshes with h ~ 4, 8, and 15 mm (total elements 4062, 1333, and 463, respectively). The two finer meshes (h = 2 and 4 mm) are the typical of those used in literature [21, 25], while the larger meshes (8, 13.3, and 20 mm) are used in this study to explore the mesh limit of the present A-FEM. The unstructured meshes of ~ 4, 8, and 15 mm were intended to check the mesh sensitivity and the robustness of the new A-FEM. Five of the discretized models (structured h = 2, 8, and 20 mm meshes and unstructured h ~ 8 and 13 mm meshes) under deformed states are shown in Figure 4 (b, c, d, e, f) with the crack trajectories roughly following the center lines of the white bands.

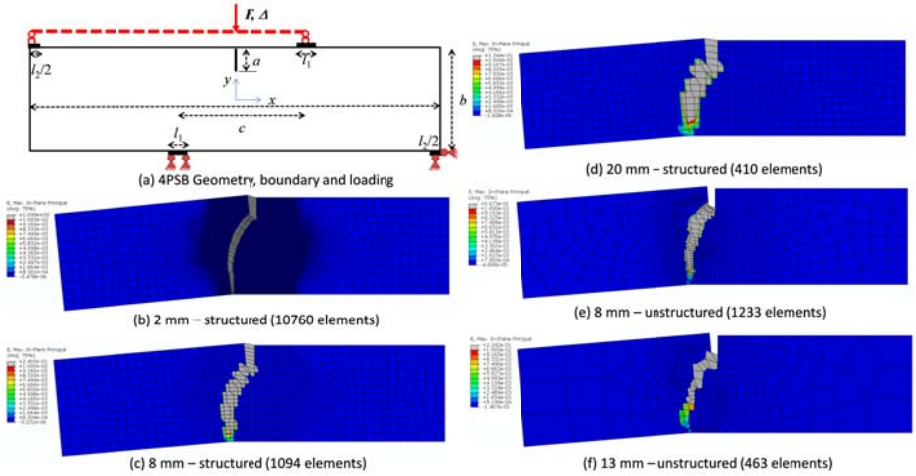

Figure 4 (a) Numerical models and simulated crack paths for structured 2mm (b), 8 mm mesh (c), and 20 mm mesh (d), and unstructured 8 mm (e) and 15 mm (f) meshes.

3.1 Mesh Sensitivity

The simulated load-displacement curves are plotted in Figure 5(a). The X-FEM prediction obtained by Moes and Belytschko [7], which used a triangular mesh of h ~ 3 mm, was superimposed on this plot for comparison (the dashed line). All curves exhibit a strong snap-back behavior. In this study, the strong snap-back behavior was captured using the arc-length method available in ABAQUS (Option RIKS).

The A-FEM computed load-displacement results are very consistent with the X-FEM result obtained in [7]. In particular, the load-displacement curves obtained with smaller mesh sizes (i.e., h = 2 mm, 4 mm, and 8 mm) are almost identical with the X-FEM results. For the larger meshes, i.e., h = 13.3 mm and 20 mm, the curves deviates mildly the finer mesh curves due to increases in initial stiffness. The systematic increase of initial stiffness with the increase of mesh sizes is largely due to the inherent numerical inaccuracy associated with the 4-node plane elements. This clearly demonstrates the mesh insensitivity of the present A-FEM.

Figure 5(b) summarizes the crack trajectories predicted by the five simulations with structured meshes. The crack paths are all very consistent and close to the experimental curve, despite they were obtained with vastly different mesh sizes. The predicted crack trajectories with the three unstructured meshes are also very consistent with those in Fig 5(b), which further demonstrates the mesh objectivity of the new A-FEM.

The insensitivity of the A-FEM to mesh structures is further demonstrated in Fig. 5(c) and Fig.

5(d). These plots compare the load-displacement curves (Fig 6c) and crack trajectories (Fig 6d) obtained with three structured meshes (4, 8 , and 13 mm) (solid lines) and those computed with unstructured meshes of similar mesh sizes (broken lines). The two sets of results are basically indistinguishable.

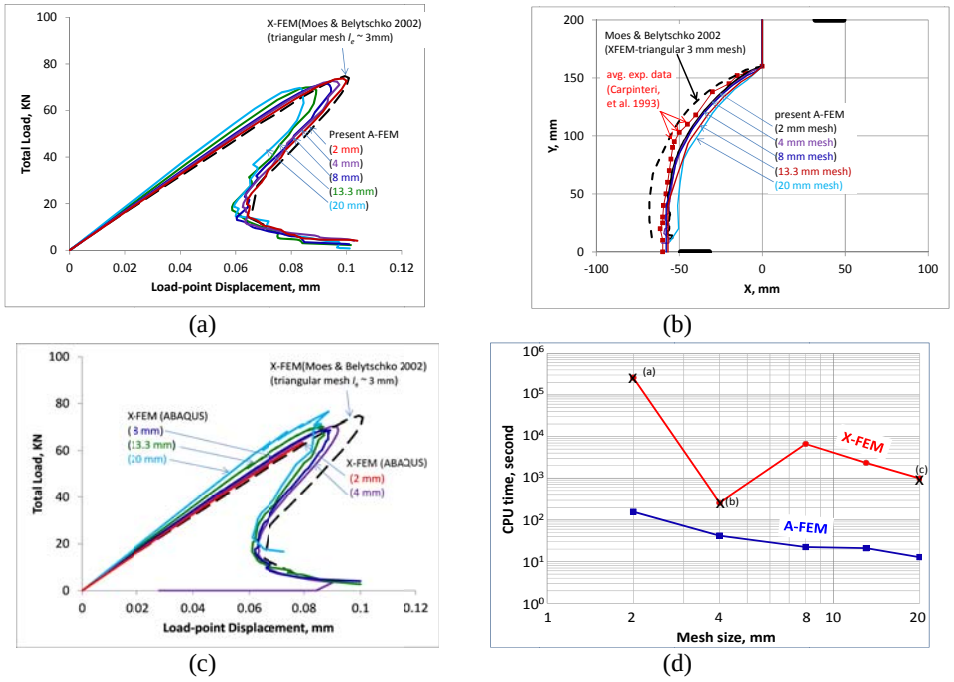

Figure 5 A-FEM simulated load-displacement curves (a) and crack trajectories (b) with the five meshes as compared to the X-FEM results and experimental results. (c) X-FEM predicted load-displacement curves compared with the A-FEM predictions. (d) Comparison of the CPU time (right vertical axis), and the numerical error (left axis) as function of mesh sizes

3.2 Numerical Efficiency and Stability as Compared to X-FEM in ABAQUS(v6.10)

In this section, the numerical accuracy, efficiency, and stability of the new A-FEM is compared against the X-FEM results obtained with ABAQUS (v6.10). Comparisons were carried out for the structure meshes only because the X-FEM failed to obtain converged solutions for any of the unstructured meshes. The meshes, boundary conditions, and loading are exactly the same as those used in previous section. All simulations were run on a Dell precision M4600 (x64 bit) mobile workstation with Intel Core i7–2860 QM CPU @ 2.5 GHz and with 8 GB of RAM.

The XFEM (ABAQUS) simulated load-displacement curves are plotted in Figure 5(c). The XFEM had enormous difficulty in completing these simulations. For the 2 mm mesh, the simulation proceeded with such a small incremental size (10^{-6} ~ 10^{-8} mm) that it had to be terminated at the displacement of 0.08 mm after 72 CPU hours of running. For the 4 mm mesh, a sudden strong snap back resulted from an incorrectly predicted crack path occurred at the displacement of 0.09 mm after the peak (Fig 5c). For the 20 mm mesh, the simulation diverged at the displacement of 0.072 mm (after snap back). For the rest cases (i.e., 8 mm and 13.3 mm mesh), the simulations were able to finish and the XFEM curves captures the peak loads and snap-back behavior reasonably well and they are close to the A-FEM results in Figure (5c).

Figure 5(d) compares the computational cost in terms of CPU time (in seconds) as functions of the mesh size. The CPU time corresponds to the point that when the displacement reached 0.1 mm (after snap-back). For the 2 mm, 4 mm, and 20 mm mesh, the X-FEM simulations were aborted due to the reasons discussed above. In these cases, the CPU times at the aborting points were taken and such data points were indicated by the X in Fig 5(d). From Figure 5(d), it is concluded that the

present A-FEM empowered by the novel condensation procedure, is at least 2 orders of magnitude more efficient than the X-FEM.

4. CONCLUSIONS

In this paper, an elemental augmentation procedure has been established to derive the augmented finite elements (A-FEs) that can accurately account for arbitrary intra-element cracks and their interaction without the need for additional external DoFs as in X-FEM or extra nodes as in PNM. It has been demonstrated that the new formulation makes it much easier in handling the multiple crack interaction problems including crack coalescence or bifurcation, since it does not require complex numerical algorithms to track the complex crack fronts.

The new A-FEM formulation does not need to assume deformation modes for elemental displacement enrichment as in the embedded discontinuity method either. Instead, it introduces internal node-pairs with normal displacements as internal nodal DoFs, which are eventually condensed at elemental level. With the proposed formulation, the crack displacements become natural outcomes of the elemental equilibrium consideration. The advantage is multi-fold. First, it enables a unified treatment of both weak and strong discontinuities. Second, for strong discontinuities with piece-wise linear constitutive relations, the new A-FEM formulation ensures an exact solution (in the piece-wise linear limit) to the condensed elemental equilibrium, which greatly improves the numerical accuracy, stability, and efficiency. Third, the unique A-FEM formulation makes it straightforward to repeat the augmentation procedure within an element to include multiple intra-element cracks, which is very powerful in dealing with multiple crack interaction problems because such augmented elements do not need extra external DoFs or nodes.

A novel elemental condensation algorithm that can provide analytical solution to local equilibrium has also been developed. The novelty in this algorithm is that, instead of assuming trial crack displacements and iterating for elemental equilibrium such as in the Newton-Raphson method, it starts with trial cohesive segments in the cohesive laws and finds the analytical solution (in piece-wise linear sense) to the elemental equilibrium through a simple consistency check. For piece-wise linear cohesive laws with only a small number of possible stiffness segments, this algorithm is very efficient.

Through the numerical examples, it has been demonstrated that the new A-FEM method, empowered by the new elemental condensation algorithm, achieved very significant improvements in numerical accuracy, efficiency, and stability. In particular, through a rigorous comparison study on a 4-point shear beam test, it has been found that the present A-FEM achieved an improvement in numerical efficiency by more than two orders of magnitude as compared to the X-FEM in ABAQUS. The A-FEM's capabilities in high-fidelity simulations of interactive cohesive cracks in heterogeneous solids have also demonstrated through the coupled debonding/kinking processes frequently observed in fiber-reinforced polymer matrix composites

Acknowledgements

Q. D. Yang acknowledges the support from the Air Force Office of Scientific Research (Dr. Ali Sayir) and NASA (Dr. Anthony Calomino) under the National Hypersonics Science Center for Materials and Structures (AFOSR Contract No. FA9550-09-1-0477). W. Liu and X. Y. Su wish to acknowledge the support from the China Scholarship Council and NSFC (Contract No. 11232001).

References

1. Cox, B.N. and Q.D. Yang, *In Quest of Virtual Tests for Structural Composites.* Science, 2006. **314**: p. 1102-1107.
2. Talreja, R., *Mulitscale modeling in damage mechanics of composite materials.* Journal of Material Science, 2006. **41**: p. 6800-6812.
3. Van de Meer, F.P. and L.J. Sluys, *Continuum Models for the Analysis of Progressive Failure in*

Composite Laminates. Journal of Composite Materials, 2009. **43**: p. 2131-2156.
4. Ha, Y.D. and F. Bobaru, *Studies of dynamic crack propagation and crack branching with peridynamics.* International Journal of Fracture, 2010. **162**: p. 229-244.
5. Silling, S.A., *Reformulation of Elasticity Theory for Discontinuities and Long-Range Forces.* Journal of the Mechanics and Physics of Solids, 2000. **48**: p. 175-209.
6. Babuška, I. and J.M. Melenk, *The partition of unity method.* International Journal for Numerical Methods in Engineering, 1997. **40**: p. 727-758.
7. Moës, N. and T. Belytschko, *Extended finite element method for cohesive crack growth.* Engineering Fracture Mechanics, 2002. **69**: p. 813-833.
8. Daux, C., et al., *Arbitrary branched and intersecting cracks with the extended finite element method.* International Journal for Numerical Methods in Engineering, 2000. **48**: p. 1741-1760.
9. Huynh, D.B.P. and T. Belytschko, *The extended finite element method for fracture in composite materials.* International Journal for Numerical Methods in Engineering, 2009. **77**: p. 214-239.
10. Song, J.H., P.M.A. Areias, and T. belytschko, *A method for dynamic crack and shear band propagation with phantom nodes.* Inter. J. Numer. Meth. Engng, 2006. **67**: p. 868-893.
11. Remmers, J.C., *Discontinuities in Materials and Structures -- A Unifying Computational Approach*, 2006, Delft University.
12. Hansbo, A. and P. Hansbo, *A finite element method for the simulation of strong and weak discontinuities in solid mechanics.* Computer Methods in Applied Mechanics and Engineering, 2004. **193**: p. 3523-3540.
13. Fang, X.J., et al., *High-Fidelity Simulations of Multiple Fracture Processes in a Laminated Composites in Tension.* Journal of the Mechanics and Physics of Solids, 2011. **59**: p. 1355-1373.
14. Ling, D.S., Q.D. Yang, and B.N. Cox, *An augmented finite element method for modeling arbitrary discontinuities in composite materials.* International Journal of Fracture, 2009. **156**: p. 53-73.
15. Budyn, E.R.L., *Multiple crack growth by the extended finite element method[D]*. 2004, Northwestern University: Evanston, Illinois.
16. Holl, M., S. Loehnert, and P. Wriggers, *An adaptive multiscale method for crack propagation and crack coalescence.* Inter. J. Numer. Meth. Engng, 2012. **in press**(DOI: 10.1002/nme.4373).
17. Alfaiate, J., G.N. Wells, and L.J. Sluys, *On the use of embedded discontinuity elements with crack path continuity for mode-I and mixed-mode fracture.* Engineering Fracture Mechanics, 2002. **69**: p. 661-686.
18. Sluys, L.J. and A.H. Berends, *Discontinuous failure analysis for mode-I and mode-II localization problems.* Int. J. Solids Struct., 1998. **35**: p. 4257–4274.
19. Linder, C. and F. Armero, *Finite elements with embedded branching.* Finite Elements in Analysis and Design, 2009. **45**: p. 280-293.
20. Dias-da-Costa, D., et al., *Towards a generalization of a discrete strong discontinuity approach.* Computational methods in Applied Mechanics and Engineering, 2009. **198**: p. 3670-3681.
21. Linder, C. and F. Armero, *Finite elements with embedded strong discontinuities for themodeling of failure in solids.* International J. Numer. Meth. Engng, 2007. **72**: p. 1391-1433.
22. Yang, Q. and M.D. Thouless, *Mixed mode fracture of plastically-deforming adhesive joints.* International Journal of Fracture, 2001. **110**: p. 175-187.
23. Yang, Q.D. and B.N. Cox, *Cohesive Models for damage evolution in laminated composites.* International Journal of Fracture, 2005. **133**(2): p. 107-137.
24. Carpinteri, A., et al., *Is mode II fracture energy a real material property?* computers and structures, 1993. **48**(3): p. 397-413.
25. Dias-da-Costa, D., et al., *An embedded formulation with conforming finite elements to capture strong discontinuities.* Int. J. Numer. Meth. Engng, 2012. **in press, DOI: 10.1002/nme.4393**.